

Spatially Resolved Mid-IR Imaging of the SR 21 Transition Disk

J.A. Eisner¹, J.D. Monnier², P. Tuthill³, S. Lacour⁴

ABSTRACT

We present mid-IR observations from Gemini/TReCS that spatially resolve the dust emission around SR 21. The protoplanetary disk around SR 21 is believed to have a cleared gap extending from stellocentric radii of ~ 0.5 AU to ~ 20 AU, based on modeling of the observed spectral energy distribution. Our new observations resolve the dust emission, and our data are inconsistent with the previous model. We require the disk to be completely cleared within ~ 10 AU, without the hot inner disk spanning ~ 0.25 – 0.5 AU posited previously. To fit the SED and mid-IR imaging data together, we propose a disk model with a large inner hole, but with a warm companion—possibly surrounded by circumstellar material of its own—residing near the outer edge of the cleared region. We also discuss a model with a narrow ring included in a large cleared inner disk region, and argue that it is difficult to reconcile with the data.

Subject headings: stars: pre-main sequence—stars: circumstellar matter—stars: individual(SR 21)—techniques: high angular resolution—techniques: interferometric

1. Introduction

While young ($\lesssim 1$ Myr) stars are generally surrounded by dust and gas rich protoplanetary disks (e.g., Koerner & Sargent 1995; McCaughrean & O’Dell 1996; Beckwith et al. 1990), these disks tend to disappear within a few million years (e.g., Haisch et al. 2001; Eisner et al. 2008). The mechanism by which protoplanetary disks are dissipated remains unclear, although several processes—including planet formation, viscous accretion onto the central star, or photo-evaporation from stellar UV and X-ray photons—may play a role (e.g.,

¹Steward Observatory, University of Arizona, Tucson, AZ 85721

²University of Michigan Astronomy Department, 941 Dennison Building, Ann Arbor, MI 48109

³School of Physics, Sydney University, N.S.W. 2006, Australia

⁴Observatoire de Paris, F-92195 Meudon, France

Calvet et al. 2002; Alexander et al. 2006; Najita et al. 2007). In any case, one expects that as protoplanetary disks evolve, they will at some point transition from being optically thick accretion disks to tenuous, optically thin disks.

Transition disks were first defined empirically based on observed spectral energy distributions (e.g., Strom et al. 1989). These objects display long-wavelength ($\gtrsim 10 \mu\text{m}$) infrared excesses indicative of optically thick disks beyond stellocentric radii of a few AU. In contrast to typical young, optically thick protoplanetary disks, however, transition disks lack opacity in the near-IR and produce less near-IR excess emission. This opacity hole is often interpreted as a region in the inner disk that is largely cleared of material.

Several systems have now been modeled in terms of this cleared inner disk picture (e.g., Calvet et al. 2002; D’Alessio et al. 2005). In addition, recent studies have found evidence that some objects appear to have hot inner disk material and optically thick outer disks, but a cleared gap at intermediate radii (e.g., Brown et al. 2007; Espaillat et al. 2008). Most of these studies are based on modeling of spectral energy distributions, although there are now a few examples where the outer edges of cleared disk regions have been imaged (e.g., Goto et al. 2006; Ratzka et al. 2007; Hughes et al. 2007; Brown et al. 2008). In addition, there are now observations of optically thin material within the “cleared” regions in some systems (e.g., Eisner et al. 2006).

SR 21 is a young star in the Ophiuchus star forming region, at an assumed distance of 160 pc. A spectral energy distribution measured from $\sim 1\text{--}100 \mu\text{m}$ shows strong mid-IR emission indicative of a disk of material that re-processes stellar emission, but a deficit of emission around $5 \mu\text{m}$. These data have been interpreted successfully with a disk model that extends from stellocentric radii of 0.25 AU to 300 AU, but with a cleared gap between 0.45 and 18 AU (Brown et al. 2007). Observations of emission from ro-vibrational transitions of CO show evidence for a narrow ring of gas near a stellocentric radius of ~ 7 AU (Pontoppidan et al. 2008), implying a substantial column of gas within the putative cleared region evinced by the SED modeling.

Detection of broad, but weak $\text{H}\alpha$ emission suggests accretion of some disk material onto the central star (Patience et al. 2008), although non-detection of $\text{Pa}\beta$ emission suggests that the accretion rate is $\lesssim 10^{-9} M_{\odot} \text{yr}^{-1}$ (Natta et al. 2006). The dust mass of the SR 21 disk has been inferred to be $\sim 2 \times 10^{-4} M_{\odot}$ (Andrews & Williams 2007; Patience et al. 2008), on the high end of the disk mass distribution for T Tauri stars (e.g., Eisner et al. 2008). Thus, while the source appears to have a fairly massive outer disk, the accretion rate is lower than that of a typical classical T Tauri star, as found for other sources classified as transition objects (Najita et al. 2007).

Here we present spatially resolved mid-IR observations of SR 21. Mid-IR observations are sensitive to scales near the outer edge of the cleared region, or even within the cleared region, and so can critically test the geometric model inferred from the spectral energy distribution. Furthermore, such observations can potentially reveal structures that might be associated with planet formation or other disk clearing processes.

2. Observations and Data Reduction

We observed SR 21 and several bright, unresolved calibrator stars at $8.8 \mu\text{m}$ (Si-2 filter) and $11.6 \mu\text{m}$ (Si-5 filter) wavelengths with the TReCS camera on the Gemini South telescope on UT 2007 May 9. To obtain diffraction limited images, we employed very short integration times to effectively freeze the atmosphere. For each source at each wavelength, we obtained 39 172-ms integrations for two sets of two up/down dither positions and two left/right nods; the total is 312 integrations per source per wavelength.

For each observed target, the data from adjacent nod positions were subtracted in order to remove the sky background. This procedure appears to work reasonably well, leaving < 300 counts RMS residual, compared to peak target fluxes of $\sim 50,000$ counts.

We analyzed the calibrated images using techniques borrowed from non-redundant aperture masking interferometry. A “pseudo-mask” consisting of 27 sub-apertures was created and we computed the visibilities for each of the 351 baselines. Because our aperture is not, in fact, non-redundant (i.e., each of our visibilities contains contributions from a number of identical baselines), each measured visibility includes redundancy noise. To calibrate this effect we computed the visibilities for a number of unresolved “check stars.” Uncertainties are largest for intermediate baselines, where photon counts are lower than for the shortest baselines but redundancy noise is higher than for the longest baselines.

We azimuthally average the 2-D visibility distributions, to enhance effective signal-to-noise and for ease of plotting. We typically use these azimuthally-averaged visibilities in the analysis below.

3. Modeling

We begin this section with a simple estimate of the size scale of the mid-IR emission seen in our observations. We then reproduce the gapped-disk model of Brown et al. (2007) and demonstrate that, while it fits the observed SED well, it does not provide a good fit to our imaging data. We then generate a new grid of models and attempt to obtain a better

fit to the combined SED+mid-IR imaging dataset.

3.1. Estimated Size of the Mid-IR Emission

To provide a rough estimate of the size scale over which the mid-IR emission seen in our observations is distributed, we fit simple, geometric ring models to the visibilities (e.g., Eisner et al. 2004). We fit the data at 8.8 μm and at 11.6 μm separately. At 8.8 μm , the visibilities are fitted well with a ring model with a radius of 11 ± 1 AU (67 ± 5 mas). At 11.6 μm , the best-fit ring model has a radius of 15 ± 1 AU (92 ± 5 mas). The data at each wavelength are fitted well with these simple models, and the fits provide reduced χ^2 values well below unity.

The emission at 8.8 μm appears significantly more compact than the emission at 11.6 μm . This is due, in part, to the larger stellar contribution to the emission at shorter wavelengths. However, if we use stellar properties from the literature (e.g., Brown et al. 2007) and account for the stellar flux at each wavelength, we still find a significantly larger angular extent of the emission at 11.6 μm compared to 8.8 μm . The larger size at longer wavelength implies a temperature gradient with cooler material distributed more widely than hot material.

We also fitted an inclined ring model (e.g., Eisner et al. 2004) to the 2-D visibilities in order to explore potential asymmetry in the data. At 8.8 μm , the best-fit model has an inclination of $26^\circ \pm 6^\circ$ and a position angle (PA, east of north) of $44^\circ \pm 7^\circ$. At 11.6 μm , the inclination is $27^\circ \pm 3^\circ$ and the PA is $61^\circ \pm 8^\circ$.

3.2. Testing the gapped-disk model

Brown et al. (2007) compiled an SED for SR 21 from ~ 1 –100 μm , and modeled it with a disk including hot material from 0.25 to 0.45 AU that reproduced the observed near-IR excess, a cleared gap extending from 0.45 to 18 AU, and cool outer disk material at larger stellocentric radii that reproduces the large far-IR luminosity of the object.

Here we reproduce the model of Brown et al. (2007). We maintain all of their assumed model parameters, except for the inclusion of mm-sized grains in the mid-plane. Since we are concerned only with the region of the disk in the vicinity of the gap we may safely ignore these large grains. We also assumed a blackbody for the stellar emission, rather than the Kurucz model used by Brown et al. (2007). While Brown et al. (2007) do not specify the radial dependence of the disk surface density assumed in their modeling, we set this as $\Sigma(R) \propto R^{-1}$. We computed an SED and images at 8.8 and 11.6 μm for this model using the

Monte Carlo radiative transfer code RADMC (Dullemond & Dominik 2004) without vertical structure iteration.

The resultant model SED is shown in Figure 1, along with the SED data from Brown et al. (2007). We are able to reproduce the previous model, and fit the SED well. However, this model does not fit our mid-IR imaging data. Figure 2 shows the visibilities predicted by this model at 8.8 and 11.6 μm . These visibilities were computed from model images using the same procedure applied to the data.

The model visibilities are clearly different than the observed visibilities. In particular, the model has a strong compact component that produces higher visibilities (with respect to the data) at the longest baselines, and an extended component that produces lower visibilities at shorter baselines. The compact component arises from the hot inner disk in the model, which extends from ~ 0.25 to 0.45 AU. The extended component corresponds to the warm inner edge of the (outer) disk and the flared outer regions. The fact that the shape of the observed visibility curves resemble those of single-component models with a size scale of ~ 10 –20 AU suggests that the hot inner disk and some of the flared outer disk may need to be eliminated from the model before it can be made consistent with the data.

3.3. Disk Models

We attempted to fit a variety of disk models to our data, generating ~ 500 models using RADMC. We varied the inner and outer disk radii, the inner and outer radii of the cleared gap, the factor by which the density in the gap is reduced, the disk mass, the power-law indices describing the disk surface density and flaring profiles, and the disk scale height. This model grid included disks that had neither gaps nor large clearings, disks with gaps, and disks with large inner clearings. We attempted to minimize the χ^2 residual between these models and our combined mid-IR imaging+SED dataset. We assumed the SED data were uncertain by 5%, and used the uncertainties in the visibilities estimated from our reduction procedure (and plotted in Figure 2).

None of the models considered provided a substantially better fit than the gapped-disk model discussed in §3.2. This is not surprising in light of the arguments given above. Disk models that include hot emission at small stellocentric radii (~ 0.25 AU) produce mid-IR emission much more compact than observed. But disk models lacking this hot, compact material, produce substantially less flux from ~ 2 –5 μm than observed in the SED.

3.4. Disk + Companion Model

Here we attempt to reconcile the observation that the SR 21 system does appear to have flux in excess of the stellar photosphere at near- to mid-IR wavelengths (as seen in the SED) with the inference (based on the mid-IR imaging data) that this flux cannot arise from the sub-AU scales expected for the inner disk. Our proposed solution is that this near- and mid-IR emission traces a warm “companion” located near the outer edge of the cleared region. Given the youth of the SR 21 system, the companion may include emission from both (sub-)stellar and circum(sub)stellar emission. We show below that as long as the emission from the companion is marginally resolved in our mid-IR imaging data (i.e., if it has a stellocentric radius of $\sim 10\text{--}20$ AU), the companion emission does not significantly affect the computed visibility curve, and a disk+companion model can approximately reproduce the available data.

We implemented this model by first generating a grid of models with large inner clearings or gaps using the RADMC code (see §3.3). We then added a companion to the model disk SEDs and images. We generated a small grid of values for the temperature, radius, and stellocentric radius of the companion, and generated models for each combination of these parameter values. We placed the companion at a position angle of 50° , following the direction of asymmetry seen in the data (§3.1), although here we azimuthally average the model visibilities and so the chosen PA is not important. The main constraints on the temperature and radius of the companion come from the near- and mid-IR excess fluxes, while the stellocentric radius of the companion is constrained (weakly) by the shape of the measured visibility curves.

This model is not fully self-consistent, since the heating from the companion is not included in the calculation of the disk temperature structure. Because the bolometric luminosity of the companion is small relative to the primary star, the additional heating that we neglect should also be relatively small. We are unable to determine rigorous error intervals for our fits because we can only consider a limited number of values for each parameter in order to keep the considered multi-dimensional parameter space within the realm of computational feasibility. Given the uncertainties in the data, we estimate parameters are uncertain by at least 10%.

The predicted SED and visibilities for our best-fitting model are shown in Figures 1–2, and we show a synthetic image at $11.6\ \mu\text{m}$ in Figure 3. The disk is cleared all the way into the central star, and this cleared region extends outward to 15 AU. The disk mass is $10^{-5} M_\odot$. This disk has a scale height of 0.10 AU, smaller than in Brown et al. (2007). All of the other disk parameters are the same as for the model in §3.2. The best-fit model has a companion with a temperature of 730 K, a radius of $40 R_\odot$, and a stellocentric radius of 18

AU. While the best-fit model places the companion slightly outside of the cleared region, within uncertainties we can not rule out the possibility that the companion resides within the clearing.

The best-fit model produces asymmetric emission because of the companion. The slight asymmetry seen in the mid-IR imaging data (§3.1) may reflect this companion flux. The position angle derived from our data is different (at the $\sim 3\sigma$ level) from the disk position angle inferred from observations of CO line emission (Pontoppidan et al. 2008), suggesting that the asymmetry in our mid-IR data may trace a non-disk (e.g., companion) component. However, the asymmetry seen in the data is smaller than we would expect from our model. If we fit the 2D visibility data directly, the preferred value for the companion’s stellocentric radius is ~ 7 AU. Given the noise in the data, especially for the 2D visibilities where we do not have the benefit of azimuthal averaging, we can not strongly constrain the position of the putative companion.

3.5. Disk + Narrow Ring

Another potential explanation of the data is a model including a large inner clearing with a narrow ring of emission at a stellocentric radius of ~ 1 AU (where disk temperatures are ~ 700 K). This ring could add mid-IR flux without substantially altering the visibilities, similar to the companion discussed above. We found, however, that such a model did not reproduce the data well. Putting the emission at about 1 AU led to more compact emission than the companion model above, and hence a worse fit to the visibilities. Furthermore, the inclusion of sufficient material to produce the correct level of flux excess led to a shadowed, and hence cooler, outer disk. The combination of these two effects led to models that do not provide good fits to the combined SED and mid-IR imaging dataset. If one forced the inner ring to lie in a geometrically thin configuration, or allowed a substantial warp between the inner ring and the outer disk, the models could potentially be made to fit better. It is unclear, however, whether such modifications are physically realistic.

4. Summary and Discussion

The model used to fit the SED of SR 21, computed by Brown et al. (2007), is not consistent with the mid-IR imaging data we obtained with TReCS. In §3.4, we argued that the SED and the mid-IR imaging data could all be explained in the context of a disk model with a large inner clearing (as opposed to a gap), and with a warm companion residing near

the outer edge of the cleared region.

Planetary or proto-planetary objects residing in the inner regions of transition disks have been proposed as a potential cause for their inner clearings (e.g., Goldreich & Tremaine 1982; Bryden et al. 1999; Rice et al. 2003). Other sources classified as transitional disks have turned out to be circumbinary disks (Guenther et al. 2007; Ireland & Kraus 2008), where the outer disk may be truncated by tidal interactions with stellar-mass companions (e.g., Lin & Papaloizou 1979).

Given the inferred temperature and radius of the companion in our model, it is unlikely to be a fully-formed star or planet. However, an accreting object could be quite warm and large as it radiates away the copious energy liberated by the infalling material. The “companion” in our model may correspond to the cloud of accreting material around a forming proto-planet or low-mass protostar. We can not constrain the stellocentric radius of the companion in our model well enough to determine whether it lies in the cleared region or in the innermost regions of the disk. If it actually resides in the disk, (as pictured in Figure 3), its large inferred temperature still lends credence to the idea that it is a self-luminous object, perhaps fueled by accreting material.

We argued above that a disk model with a large inner clearing that contains ring-like emission within the cleared region is difficult to reconcile with the data. However, if a mechanism could be found that would prevent the inner disk material from casting a shadow over the outer disk—for example, if the matter was confined to a vertically-thin or highly inclined ring—then such a model could potentially fit the data. The inference of a ring of gas near a stellocentric radius of ~ 7 AU (Pontoppidan et al. 2008) provides some support for such a model, although this gaseous ring could also be explained in the context of sculpting by a companion.

High angular resolution imaging of SR 21 at shorter wavelengths is needed to further elucidate the nature of the emission within the “cleared” inner disk region. Such observations can have higher resolution than those presented here and would be more sensitive to the warm companion (or other matter) inferred to reside in the inner disk. Our models predict that in the K -band the companion has $\sim 5\%$ the flux of the central star. In the L -band, the companion has $\sim 25\%$ the flux. At still longer wavelengths, the brightness ratio between the companion and the star increases, but the disk also brightens considerably, making detection of the companion more difficult. The inferred stellocentric radius of the companion places it $\lesssim 100$ mas away from the central star, although our constraints on the stellocentric radius are weak and it could be closer to the star. The companion posited in our model may be detectable in near-IR (K and L) adaptive optics observations, providing a potential test of the models presented in this paper.

Based on observations obtained at the Gemini Observatory. We are grateful to Kevin Volk, Tom Hayward, Adwin Boogert, Chris Packham, and Charles Telesco for making these observations possible. We also thank Kees Dullemond for providing us with the RADMC code, and helping us to get it running. JDM acknowledges support from NASA-Origins NNG05G180G and nsf-ast0352723.

REFERENCES

- Alexander, R. D., Clarke, C. J., & Pringle, J. E. 2006, *MNRAS*, 369, 216
- Andrews, S. M. & Williams, J. P. 2007, *ApJ*, 671, 1800
- Beckwith, S. V. W., Sargent, A. I., Chini, R. S., & Guesten, R. 1990, *AJ*, 99, 924
- Brown, J. M., Blake, G. A., Dullemond, C. P., Merín, B., Augereau, J. C., Boogert, A. C. A., Evans, II, N. J., Geers, V. C., Lahuis, F., Kessler-Silacci, J. E., Pontoppidan, K. M., & van Dishoeck, E. F. 2007, *ApJ*, 664, L107
- Brown, J. M., Blake, G. A., Qi, C., Dullemond, C. P., & Wilner, D. J. 2008, *ApJ*, 675, L109
- Bryden, G., Chen, X., Lin, D. N. C., Nelson, R. P., & Papaloizou, J. C. B. 1999, *ApJ*, 514, 344
- Calvet, N., D’Alessio, P., Hartmann, L., Wilner, D., Walsh, A., & Sitko, M. 2002, *ApJ*, 568, 1008
- D’Alessio, P., Hartmann, L., Calvet, N., Franco-Hernández, R., Forrest, W. J., Sargent, B., Furlan, E., Uchida, K., Green, J. D., Watson, D. M., Chen, C. H., Kemper, F., Sloan, G. C., & Najita, J. 2005, *ApJ*, 621, 461
- Dullemond, C. P. & Dominik, C. 2004, *A&A*, 421, 1075
- Eisner, J. A., Chiang, E. I., & Hillenbrand, L. A. 2006, *ApJ*, 637, L133
- Eisner, J. A., Lane, B. F., Hillenbrand, L., Akeson, R., & Sargent, A. 2004, *ApJ*, 613, 1049
- Eisner, J. A., Plambeck, R. L., Carpenter, J. M., Corder, S. A., Qi, C., & Wilner, D. 2008, *ApJ*, 683, 304
- Espaillet, C., Calvet, N., Luhman, K. L., Muzerolle, J., & D’Alessio, P. 2008, *ApJ*, 682, L125

- Goldreich, P. & Tremaine, S. 1982, *ARA&A*, 20, 249
- Goto, M., Usuda, T., Dullemond, C. P., Henning, T., Linz, H., Stecklum, B., & Suto, H. 2006, *ApJ*, 652, 758
- Guenther, E. W., Esposito, M., Mundt, R., Covino, E., Alcalá, J. M., Cusano, F., & Stecklum, B. 2007, *A&A*, 467, 1147
- Haisch, K. E., Lada, E. A., & Lada, C. J. 2001, *ApJ*, 553, L153
- Hughes, A. M., Wilner, D. J., Calvet, N., D’Alessio, P., Claussen, M. J., & Hogerheijde, M. R. 2007, *ApJ*, 664, 536
- Ireland, M. J. & Kraus, A. L. 2008, *ApJ*, 678, L59
- Koerner, D. W. & Sargent, A. I. 1995, *AJ*, 109, 2138
- Lin, D. N. C. & Papaloizou, J. 1979, *MNRAS*, 186, 799
- McCaughrean, M. J. & O’Dell, C. R. 1996, *AJ*, 111, 1977
- Monnier, J. D. 2007, *New Astronomy Review*, 51, 604
- Najita, J. R., Strom, S. E., & Muzerolle, J. 2007, *MNRAS*, 378, 369
- Natta, A., Testi, L., & Randich, S. 2006, *A&A*, 452, 245
- Patience, J., Akeson, R. L., & Jensen, E. L. N. 2008, *ApJ*, 677, 616
- Pontoppidan, K. M., Blake, G. A., van Dishoeck, E. F., Smette, A., Ireland, M. J., & Brown, J. 2008, *ApJ*, 684, 1323
- Ratzka, T., Leinert, C., Henning, T., Bouwman, J., Dullemond, C. P., & Jaffe, W. 2007, *A&A*, 471, 173
- Rice, W. K. M., Wood, K., Armitage, P. J., Whitney, B. A., & Bjorkman, J. E. 2003, *MNRAS*, 342, 79
- Strom, K. M., Strom, S. E., Edwards, S., Cabrit, S., & Skrutskie, M. F. 1989, *AJ*, 97, 1451

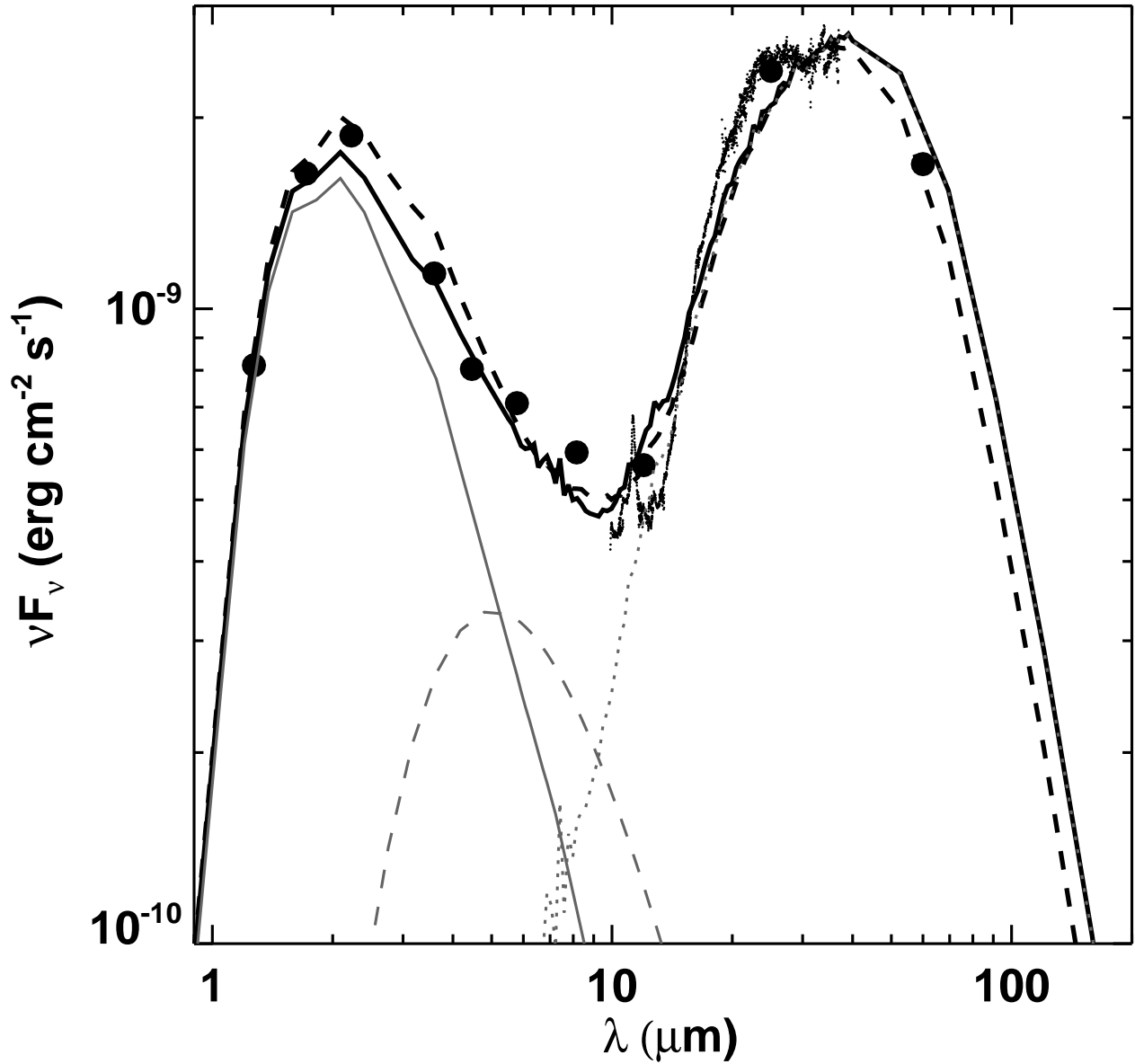


Fig. 1.— Observed SED for SR 21 (broadband photometry: *large points*; IRS spectrum: *small points*) with model predictions overplotted. We show the SED for a model that nearly matches the one derived previously by Brown et al. (2007) (*dashed black curve*), as well as for the disk+companion model described in §3.4 (*solid black curve*). The stellar contribution to both models is shown with the solid gray curve. The contribution from the companion and from the outer disk in the disk+companion model are shown with a dashed gray curve and with a dotted gray curve, respectively. The parameters of these models are given in the text.

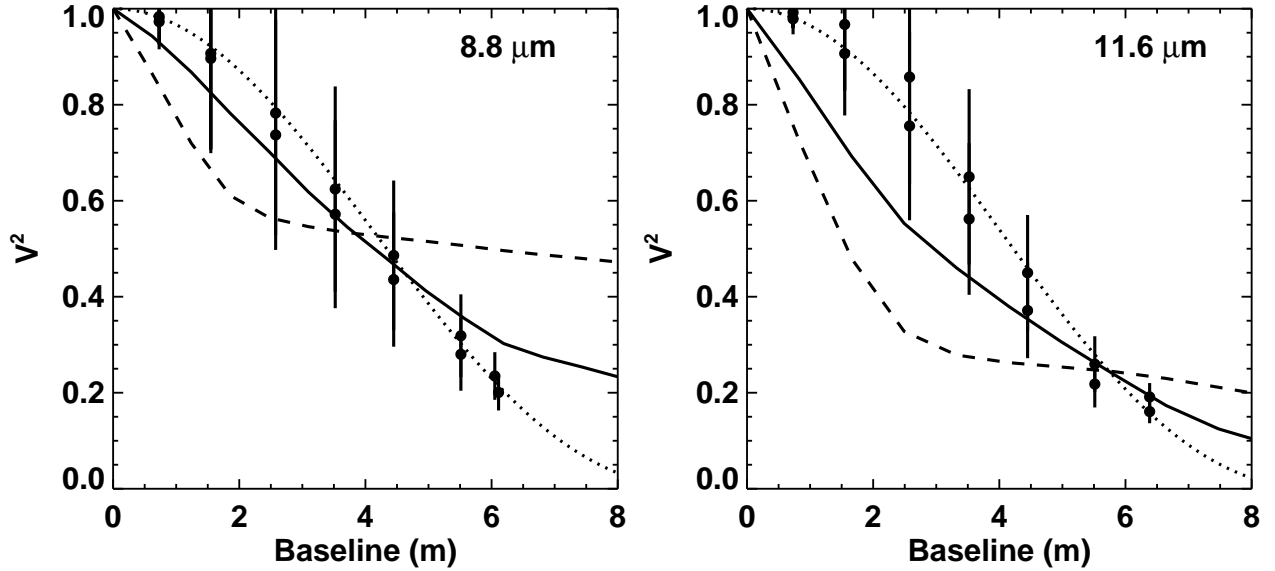


Fig. 2.— Mid-IR squared visibilities computed from our short-exposure images from TReCS (*points*) with the predictions of several models. The two sets of points represent two datasets taken ~ 2 minutes apart. The visibilities predicted by the SED-based, gapped disk model of Brown et al. (2007) are shown with the dashed curve. The solid curve shows the visibilities expected for the disk+companion model described in §3.4; this model was fitted to the mid-IR visibility data and SED data simultaneously. We also show the visibilities for simple ring models that were fitted separately to the visibility data at each observed wavelength (§3.1). The observed and predicted visibilities plotted here have all been azimuthally averaged.

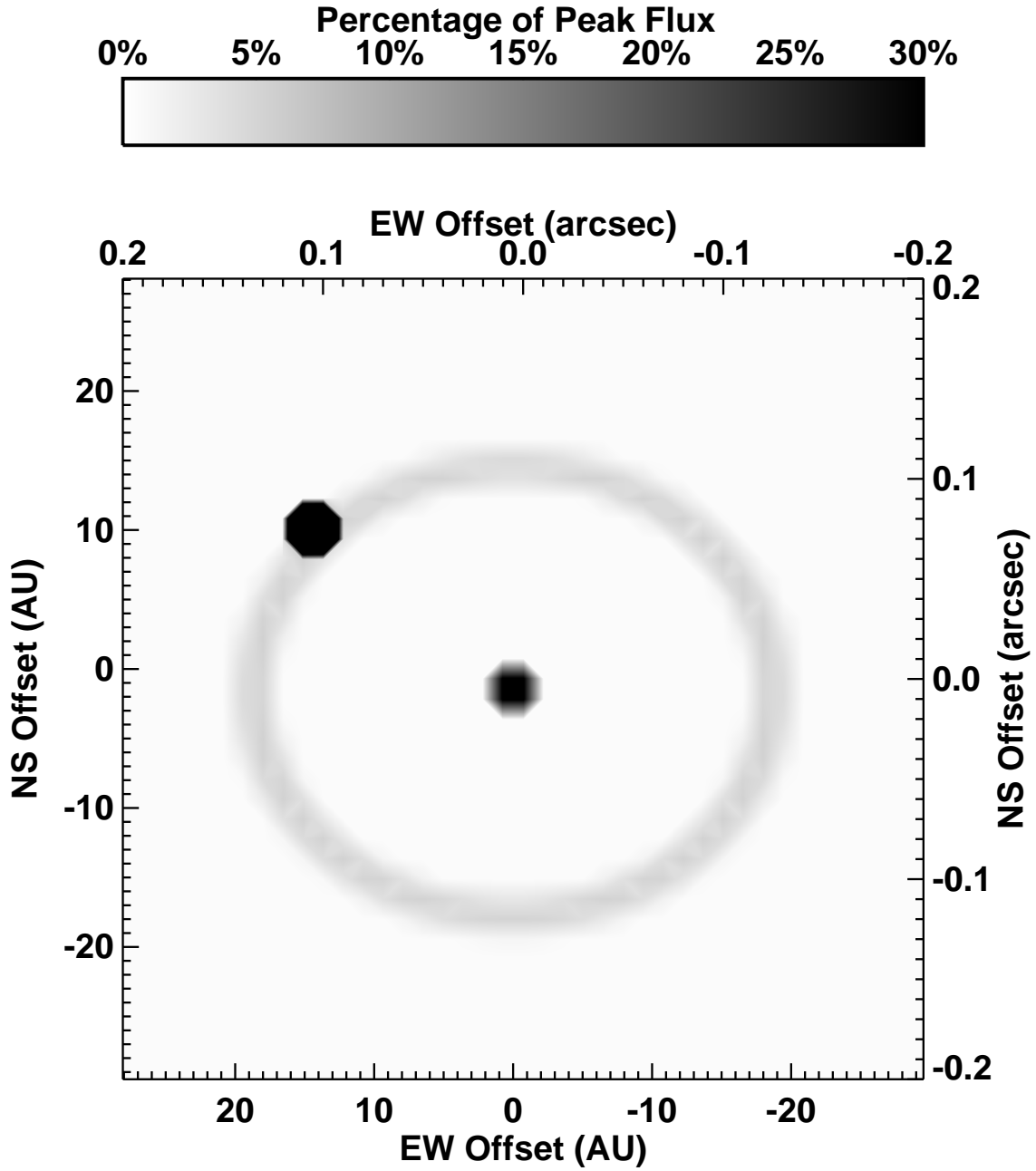


Fig. 3.— A synthetic image of our disk+companion model (§3.4) at $11.6 \mu\text{m}$ wavelength. We show only the inner $100 \text{ AU} \times 100 \text{ AU}$ of the images, to highlight the structure near the cleared inner region. Note that the exact location of the companion is not well-constrained, and while the best-fit model puts the companion within the outer disk, a location well within the cleared region is compatible with our data.